Overcoming the Interfacial Challenges of $LiFePO_4$ in Inorganic All-Solid-State Batteries

Ashley Cronk[a], Yu-Ting Chen[a], Grayson Deysher[a], So-Yeon Ham[a], Hedi Yang[b], Phillip Ridley[b], Baharak Sayahpour[a], Long Hoang Bao Nguyen[b], Jin An Sam Oh[b], Jihyun Jang[b], Darren H. S. Tan[b], and Ying Shirley Meng[b,c,]**

[a] Materials Science and Engineering Program, University of California San Diego, La Jolla, CA, 92093, United States

[b] Department of NanoEngineering, University of California San Diego, La Jolla, CA, 92093, United States

[c] Pritzker School of Molecular Engineering, The University of Chicago, Chicago, IL, 60637, United States

Corresponding Author

* Ying Shirley Meng, E-mail: shirleymeng@uchicago.edu

* Darren H.S. Tan, E-mail: dht020@eng.ucsd.edu

ABSTRACT

All-solid-state batteries (ASSBs) are one of the most promising systems to enable long-lasting and thermally resilient next-generation energy storage. Ideally, these systems should utilize low-cost resources with reduced reliance on critical materials. Pursuing cobalt- and nickel-free chemistries, like $LiFePO_4$ (LFP), is a promising strategy. Morphological features of LFP essential for improved electrochemical performance, are highlighted to elucidate the interfacial challenges when implemented in ASSBs, since adoption in inorganic ASSBs have yet to be reported. In this work, the compatibility of LFP with two types of solid-state electrolytes, Li_6PS_5Cl (LPSCl) and Li_2ZrCl_6 (LZC), are investigated. The potential existence of oxidative decomposition products is probed using a combination of structural, electrochemical, and spectroscopic analyses. Bulk and interfacial characterization reveal that the sulfide-based electrolyte, LPSCl decomposes into insulative products, and electrochemical impedance spectroscopy is used to quantify the resulting impedance growth. However, through utilization of the chloride-based electrolyte, LZC, high-rate and stable electrochemical performance is achieved at room temperature.

TOC GRAPHICS

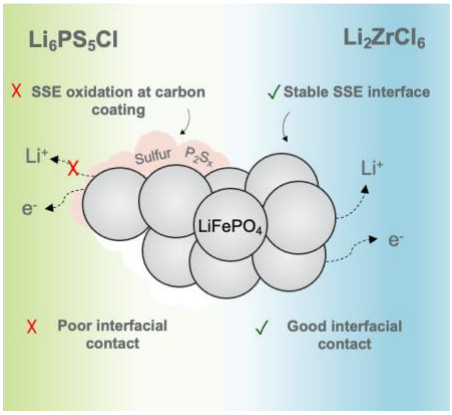

After several decades of development, lithium-ion batteries have made monumental breakthroughs in both energy densities and cycle life. This has enabled their extensive market dominance in nearly all consumer devices and is now seeing extensive implementation in emerging applications, such as electric vehicles and stationary storage devices.[1,2] These performance improvements have been largely attributed to advancements in state-of-the-art commercial cathode materials, such as high-capacity lithium nickel cobalt manganese oxide (NCM) or nickel cobalt aluminum (NCA) cathodes, which are commonly used in electric vehicles or high voltage lithium cobalt oxide (LCO), commonly used in portable devices. However, the combined effects of rapidly growing demand, along with the limited availabilities and supply chain resource challenges of nickel (Ni) and cobalt (Co) mining have resulted in rising costs and shortages for these critical materials.[3] The problem, also exacerbated by the recent pandemic, has resulted in more than 430% and 125% increase in Ni and Co in prices per ton between 2020 and 2022.[4] While some believe this increase to be transient in nature leading to an eventual decrease, fundamental trends in sheer demand and limited supply of such critical materials have compelled manufacturers to explore cathode alternatives that overcome these supply and scarcity challenges. Next-generation energy storage systems should capitalize on low-cost abundant materials with reduced impact from supply chain fluctuations.[5] Thus, the lithium iron phosphate (LFP) cathode, first reported by Goodenough et al.[6] in 1997, has been extensively explored due to its negligible toxicity and high-rate capability. Recently, original equipment manufacturers have also announced plans for the adoption of LFP cathodes in their products, eliminating their reliance on conventional Ni- or Co- containing materials.[7,8] Furthermore, LFP-based chemistries are projected to account for 42% of the battery demand by 2030 with the global demand expected to grow by thirteen times, exceeding 1 TWh by 2035.[9,10]

Market outlooks coupled with the growing demand for electrified transport and grid storage, advocate for LFP to become one of the dominant cathode materials employed for most energy storage applications.

LFP exhibits an olivine crystal structure, facilitating one-dimensional lithium diffusion during (de)lithiation[11], where a two-phase reaction exists during the conversion of lithiated LFP to delithiated $FePO_4$.[12] Additionally, its strong P-O covalent bonds make LFP one of the safest commercialized cathodes.[11] LFP alleviates many of the safety concerns arising from conventional NCM or LCO type cathode materials that undergo thermal runaway at high temperatures.[13] However, safety hazards can still be present when using LFP, but only due to the commonly used highly flammable liquid organic electrolytes. Solid electrolytes can offer a safer alternative. Interestingly, research efforts on LFP in solid-state batteries have mainly utilized organic polymer electrolytes which can still exhibit some degree of flammability. Prior studies using LFP cathodes have mainly relied on polymer hybrid electrolytes or gel-type slurries.[14–26] While categorized as solid-state, polymer electrolytes still exhibit vital disadvantages such as their low ionic conductivities and the use of flammable organic additives. The low room temperature ionic conductivities of the solid polymer electrolytes are usually mitigated by high-temperature operation, which is a prevalent strategy used amongst prior works.[14,15,17,18,19,22,23,25,26] However, relying on high-temperature environments is not desirable for most energy storage applications. The use of oxidatively stable and conductive inorganic solid electrolytes that can enable the use of LFP at room temperature has yet to be reported.

Amongst the inorganic solid-state electrolytes (SSEs) previously investigated for ASSBs, argyrodite Li_6PS_5Cl (LPSCl) is a popular candidate due to its high room temperature ionic conductivity (>1 mS cm^{-1}),[27] improved deformability (Young's Modulus of 30 GPa) compared

to popular oxides, and dry room processing stability.[28,29] LPSCl possesses some drawbacks as well, such as poor interfacial stability due to its narrow electrochemical window[30], making cathode coatings a widely adopted strategy to mitigate LPSCl oxidation.[31] Despite having a low oxidation potential, LPSCl SSEs have been successfully paired against higher voltage (~4 V) cathodes like LCO or NMC, demonstrating the effectiveness of protective coating layers.[32–34] However, despite the lower operating voltage of LFP cathodes (3.5 V), there have been no studies to date on the compatibility of LFP against common inorganic SSEs such as LPSCl, with or without protective coating layers. Nonetheless, enabling cathodes in ASSBs without use of coating is still preferred. Therefore, SSEs with both favorable mechanical properties and improved electrochemical stability remains of interest to the field.

Recently, chloride-based SSEs have become an attractive candidate due to their high oxidation stability limits,[35] high room temperature ionic conductivities, along with favorable mechanical properties.[36,37] Early chloride SSEs reported include ternary compounds like Li_3YCl_6[38] and Li_3InCl_6[39] which, while oxidatively stable and highly conductive, still rely on costly elements. Various quaternary compositions have also been reported with the aim to increase ionic conductivity and reduce the use of expensive elements by creating disordered electrolyte structures.[40–42] A low-cost and earth-abundant alternative containing only zirconium, Li_2ZrCl_6 (LZC), exhibits comparable room temperature ionic conductivity with other reported chlorides ($0.4 - 0.8$ mS cm^{-1}).[40,44] Additionally, its relatively high oxidation potential of 4.5 V (vs. Li/Li^+) makes it a suitable material to compare to the commonly used sulfide-based LPSCl. Therefore, LZC was selected as the SSE candidate for our study with LFP cathodes.

Herein, we report ASSBs capitalizing on a chloride-based LFP cathode composite, where no solvents, gel, or organic-based dispersant was used. We highlight the unique morphological and electrochemical properties of LFP, specifically its nanostructured features along with its carbon coating that requires the use of chloride-based SSEs to operate effectively. By investigating the interfacial stability of LFP cathodes against the commonly used sulfide-based electrolyte LPSCl, we demonstrate the intrinsic incompatibility of LFP against sulfide-based SSEs, despite the lower operating voltage of LFP compared to traditional NCM-type cathodes. This study provides insights into cathode composite design, especially when balancing the unique characteristics of cathode materials (i.e., morphology and SSE electrochemical stability) against a catholyte. The methodology used in this work connects SSE decomposition products to the impedance growth at the SSE/cathode interface. Ultimately, by capitalizing on the oxidatively stable LZC, high-rate capability at 2C and stable cycling (80% retention after 1000 cycles at 1C) was achieved at room temperature.

To verify the structural and electrochemical properties of LZC and LPSCl, X-ray diffraction was performed on the electrolytes for LZC (**Figure S1a**) with Rietveld refinement for LPSCl (**Figure S1b**). The conductivities of solid-state catholytes were measured and the resulting Nyquist plots are shown in **Figure S1c**; LZC and LPSCl exhibit ionic conductivities of 0.7 and 1.3 mS cm^{-1}, respectively. Direct current polarization was conducted to determine the electronic conductivity (**Figure S1d)** where LZC and LPSCl result in 8×10^{-9} S/cm and 1.6×10^{-8} S/cm, respectively. To highlight the drastic differences in electrolyte electrochemical stabilities, linear sweep voltammetry (LSV) was conducted to determine the electrochemical stability window (**Figure 1a)**. Oxidative sweeps to 5 V (vs. Li/Li^+) highlight the clear challenge of using LPSCl within the cathode composite, oxidation occurs near 2.3 V, where two oxidation peaks are

observed at 2.3 V and 2.7 V, respectively. These results align well with the predicted oxidative decomposition of LPSCl to elemental sulfur, LiCl, and Li-P_2S_x species,[45] determined from first-principles calculations. To characterize electrolyte oxidation under comparable cell cycling conditions, specifically during the 0.1 mA cm^{-2} constant current charge to 4 V, electrolyte/carbon composite cathodes were used as the working electrode and LiIn as the counter electrode. During the charging process, significant capacity was obtained due to the decomposition of LPSCl, which began at 2.3 V (**Figure 1b**), aligning well with the electrochemical stability window measurements obtained in **Figure 1a**. A total charge capacity of 407.2 mAh g^{-1} was obtained, close to the theoretical capacity of 499.1 mAh g^{-1} for LPSCl.

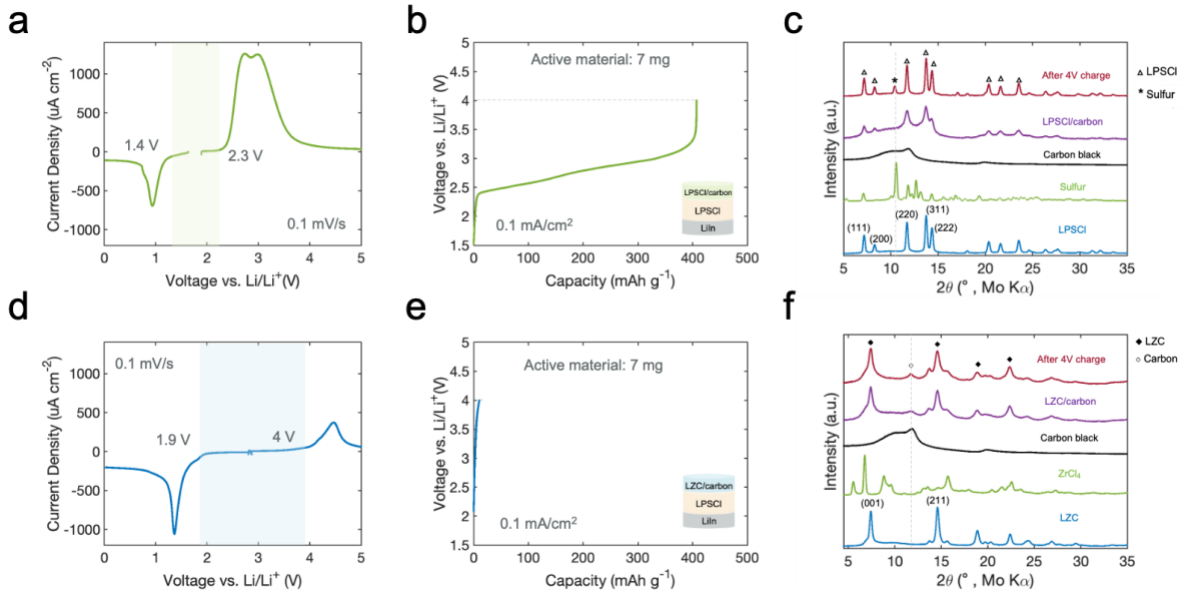

Figure 1. Linear sweep voltammetry, constant current charge behavior, and X-ray diffraction spectra of charged a), b), c) LPSCl and d), e), f) LZC where the shaded region in a) and d) represent the electrolyte stability window.

Post-mortem analysis was conducted on the charged electrolyte/carbon composites where bulk properties were determined by X-ray diffraction (XRD) (**Figure 1c and 1f**) and interfacial

products detected with Raman spectroscopy (**Figure S2)**. After the 4 V charge, elemental sulfur was detected in the XRD spectra where the main diffraction peak of (222) is observed at 10.53º 2θ (**Figure 1c**). The presence of elemental sulfur is further reinforced by the complementary Raman spectra, which displays peaks associated with vibrational modes evident of elemental sulfur at 154 cm^{-1}, 218 cm^{-1}, and 472 cm^{-1} as shown in **Figure S2a**.

In contrast to LPSCl, the LZC oxidation sweep shows decomposition beginning at 4 V (**Figure 1d**) from the expected formation of Cl_2 (g) and $ZrCl_4$, while the reduction sweep to 0 V shows decomposition at 1.9 V attributed to the reduction of Zr^{4+} to metallic Zr. These results align well with LZC phase equilibria and first-principles calculations.[44] Further, LZC shows negligible capacity contribution during the charge process as shown in **Figure 1e**, agreeing well with the obtained current density in the electrochemical stability window. XRD spectra of the charged LZC composite show no changes or evolution of new diffraction peaks observed after the 4 V charge (**Figure 1f**), reinforcing the oxidation stability of the chloride-based electrolyte. Rietveld refinement was conducted on the LZC/carbon composites where lattice parameters remained consistent after the 4 V (vs. Li/Li^+) charge as shown in **Figure S3.** No identifiable signature was detected on the Raman spectra of pristine and charged LZC (**Figure S2b**), as vibrational peaks from LZC might exhibit low Raman activities which can be masked easily by the amorphous carbon. Overall, these results reinforce the disparities in electrolyte stability and capacity contributions between LPSCl and LZC. In addition, it also highlights the instability of LPSCl under oxidative conditions compared to LZC. The determined electrolyte stability windows reveal the lower oxidation stability of LPSCl, while LZC is highly stable up to 4 V, beyond the operating voltage of LFP, and is thus ideal as a solid-state electrolyte material for this system. Lastly, the post-mortem analysis results indicate that during the charged state, insulative

oxidation products of LPSCl, mainly consisting of elemental sulfur, are generated and may hinder electrochemical performance including capacity utilization and cell polarization.

Beyond electrochemical stability, solid-state systems also require good contact between cathode and SSE solid particles to facilitate lithium-ion diffusion and to reduce interfacial resistance. Since the cathode active materials are constrained by the solid-state electrolyte, volume changes and internal pressure changes require compliant solid-state electrolytes. These critical interfaces within solid-state systems have previously been systematically reviewed,[47] where good electrolyte deformability was shown to be a key factor in addition to electrochemical stability and ionic conductivity. Sufficient deformability demands high densification under fabrication pressures, creating minimal voids and better ionic connectivity throughout the cathode composite. To evaluate the densification properties of LZC and LPSCl, pellets were cold pressed under the typical cathode uniaxial fabrication pressure of 375 MPa, following procedures outlined in the experimental methods. After densification, *ex-situ* cross-section images were taken to evaluate the two-dimensional (2D) porosity.

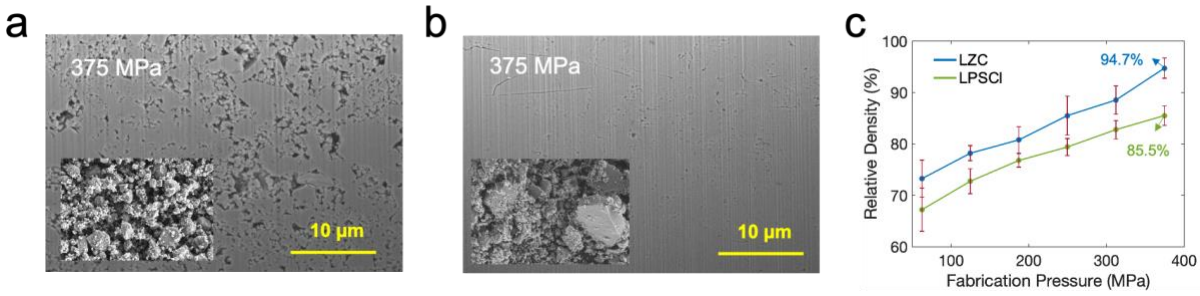

Figure 2. FIB cross-sections of cold-pressed pellets with inset showing SEM of particles at 10 µm scale of a) LPSCl and b) LZC. c) Relative density vs. fabrication pressure for LPSCl and LZC electrolytes.

For the LPSCl electrolyte, clear evidence of voids is present within the bulk (**Figure 2a**), compared to the LZC case which shows a highly dense surface (**Figure 2b**). 2D porosity was calculated using image binarization and pixel classification resulting in values of 14.5% and 3.7%, for LPSCl and LZC respectively, as shown in **Figure S4**. SEM images of the loose powders were also obtained to investigate if particle size distribution had an effect. Interestingly, LPSCl possesses smaller particles, < 2 μm with a more uniform size distribution compared to LZC. We can see from the inset image in **Figure 2b**, LZC exhibits a wider particle size distribution (< 10 μm), which may assist in its improved densification properties compared to LPSCl.

Relative density versus fabrication pressure was also evaluated to compare electrolyte densification trends (**Figure 2c**). LZC achieves an overall higher relative density, where at the typical cathode fabrication pressure of 375 MPa, 94.7% density is attained, agreeing well with the 2D porosity calculations. Comparatively, LPSCl reaches 85.5% density which supports the 2D porosity calculation and prior work studying LPSCl densification and its relative density.[48] Focused ion beam (FIB) cross-sectional images and electron dispersive spectroscopy (EDS) mapping were also obtained for the LFP/SSE cathode composite in their pristine state (**Figure S5**) where improved contact between the LFP particles and SSE was observed for the LZC case. In addition, the calculated porosity of 17% and 12% for LPSCl and LZC composites, reinforces the variance in mechanical and densification properties. These results suggest that the LZC electrolyte system enables better interfacial contact than LPSCl, an important feature when utilizing nanoscale cathode particles like LFP where surface contact is vital for good performance.

After establishing the oxidative stability and densification properties of both SSEs, cell-level electrochemical evaluation was conducted to observe how these varying properties affect electrochemical performance. The voltage profile for LFP/LPSCl cathode composite shows electrolyte oxidation during the first charge where a charge capacity of 114.3 mAh g^{-1} is obtained (**Figure 3a**) with a corresponding low discharge capacity of 46.1 mAh g^{-1}. Subsequent cycles are highly polarized with even lower LFP utilization. This is likely caused by impedance growth due to the formation of LPSCl oxidation products during the initial charge, which were shown to form beginning at 2.3 V, well before the LFP electrochemical reaction voltage. Approximately, 21.6% of this capacity is attributed to LPSCl oxidation, catalyzed by the high surface area carbon coated LFP. After oxidative decomposition products were formed, lithium transport is likely inhibited, which can explain the low initial Coulombic efficiency (ICE) of 40.3%. However, with the LZC catholyte, little to no electrolyte oxidation is observed during the first charge and very low polarization is observed in subsequent cycling. A higher charge capacity of 148.1 mAh g^{-1} and discharge capacity of 133.4 mAh g^{-1} is obtained with an ICE of 90.1% (**Figure 3b**). Similar ICE of 91.3% is obtained in a liquid electrolyte system (**Figure S6c**) where an LFP electrode with a comparable areal capacity of 1 mAh cm^{-2} was evaluated to study the losses between the liquid and solid-state system. For more practical applications, a full cell using a silicon anode was assembled at the 3.5 mAh cm^{-2} level, where comparable capacities and ICE was obtained as shown in **Figure S7**. This reinforces the stability of LZC and shows that with proper electrolyte selection similar performance to the liquid system can be achieved in ASSBs.

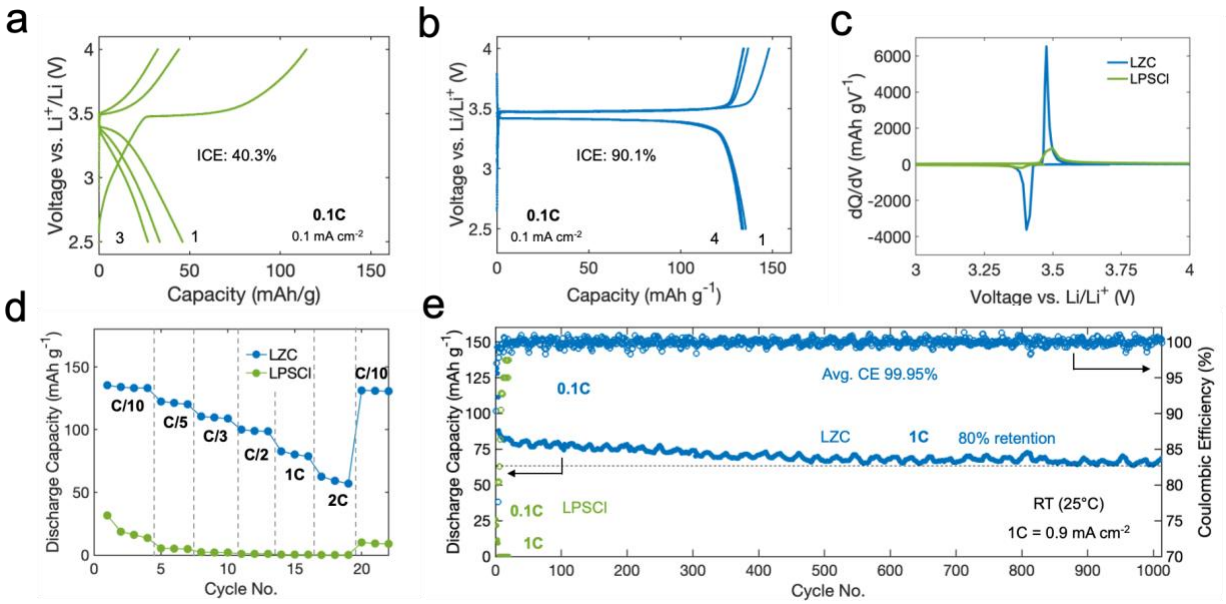

Figure 3. Electrochemical performance of LFP composite half cells. Voltage profiles at 0.1 mA cm^{-2} with a) LPSCl and b) LZC, c) Differential capacity plots of first cycle voltage profile, d) rate capability, and e) long-term cycling performance for LPSCl and LZC cells.

Differential capacity analysis was also conducted from the first cycle voltage profile of LPSCl and LZC (**Figure 3c**), where capacity is obtained using LPSCl before the two-phase LFP transition at 3.5V, another indication of electrolyte oxidation. Rate capability testing was conducted up to a rate of 2C where capacity of 65 mAh g^{-1} is attained with LZC, followed by a full discharge capacity recovery after returning to 0.1C (**Figure 3d**). Long-term cycling stability was also evaluated. Under 1C (0.9 mA cm^{-2}) cycling conditions, 80% capacity retention was obtained after 1000 cycles at room temperature (**Figure 3e**). A relatively low-capacity utilization is observed at higher C-rates, which is likely due to the lower room temperature ionic conductivity of LZC (~10^{-4} S cm^{-1}), inducing higher cell polarization for higher current densities. This can potentially be alleviated with the use of dopants to increase the ionic conductivity of the chloride SSE, which has been previously shown to increase ionic

conductivities by up to an order of magnitude.[40–42] For the LPSCl case, little to no capacity is obtained under any elevated rate conditions due to the expected oxidation products and resulting impedance growth at the LFP/SSE interface. The continuous interfacial electrochemical reactions are further reinforced by the low coulombic efficiencies during cycling.

LFP particles are typically nano-sized and are coated in carbon as shown in **Figure S6b**. While improvements in electronic conductivity was realized due to particle size reduction to the nanoscale, nanoparticles can pose significant interface challenges when paired with SSEs that exhibit poor electrochemical stability. This is due to the high surface area contact paired with the electronically conductive carbon that assists in the electrolyte oxidation, as discussed in prior works[49] and shown in **Figure 1** where large capacity was attained with LPSCl/carbon composites (**Figure 1c**). To evaluate how the amount of carbon coating affects interfacial decomposition, elemental analysis was conducted to quantify the weight percentage of carbon at the surface of the LFP cathode where 1.6 wt.% of carbon was measured. Therefore, the total weight and volume percentage of coated carbon within the LFP/SSE composites used in this work is 0.62 wt.% and 0.78 vol.%, respectively. This means that < 1 wt.% and vol.% of carbon on the LFP particle surface can cause excessive decomposition when paired with LPSCl. For comparison, the volume percentage of the carbon additive VGCF within the cathode composite is much higher near 4 vol.%, highlighting how high surface area carbon coatings will accelerate the formation of decomposition products of SSEs unstable at the cathode operating voltage and further reinforcing the need for stable electrolytes to combat this challenge. These results also reinforce why LFP is less compatible with sulfide-based electrolytes versus other cathode materials like LCO or NMC, which are typically coated with electronically insulating layers and operate at higher charge voltages.

To characterize decomposition and local bonding environments on the cathode composite surface, X-ray photoelectron spectroscopy (XPS) was used to probe the LFP/SSE cathode composite at the charged state. The sulfur 2p spectra after the 4 V charge shows peaks which can be assigned to P_2S_x species and elemental sulfur (**Figure 4a**) based on previous work.[50] These results support the SSE oxidation products that were detected from the SSE/carbon composite post-mortem analysis in **Figure S2**. Some P_2S_x species were also present in the pristine LFP/LPSCl composite, most likely attributed to chemical side reactions when in contact with the high surface area carbon-coated LFP. The phosphorus 2p region shows both PS_4^{3-} and P=O signatures in the pristine state attributed to LPSCl and LFP (**Figure 4b**). After charging, P_2S_x species are also detected in the P 2p spectra with additional phosphate species. Upon consecutive cycling, it would be anticipated that these insulative oxidation products would be continually formed at the LFP/SSE and or carbon/SSE interface. For the LZC case, zirconium 3d (**Figure 4c**) and chlorine 2p (**Figure 4d**) spectra were collected where no changes in binding energies or evolution of new species were observed after charging. This further reinforces that the LFP/LZC cathode composite experienced little to no oxidation under these conditions.

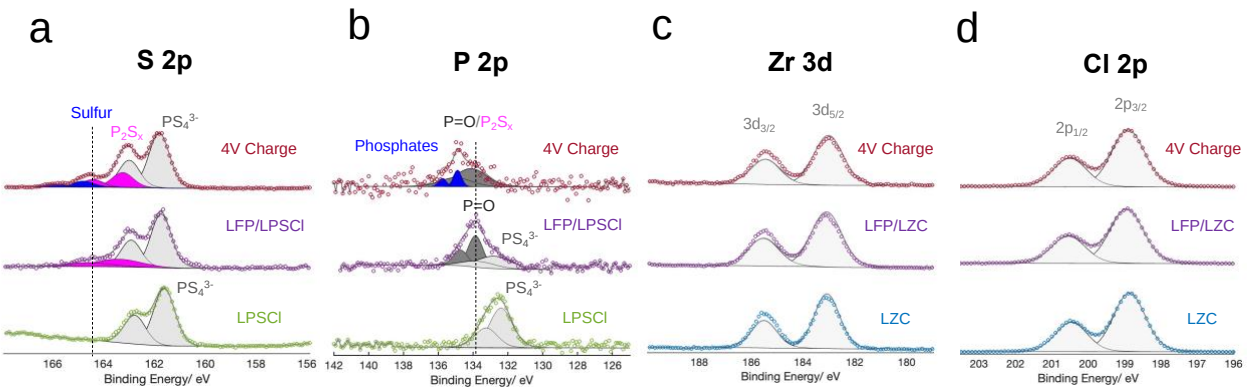

Figure 4. a) S 2p and b) P 2p XPS spectra for LPSCl, pristine composite, and after 4 V charge. c) Zr 3d and d) Cl 2p XPS spectra for LZC, pristine composite, and after 4 V charge.

The bulk properties of these charged cathode composites were also analyzed at various degrees of de-lithiation. XRD patterns of the LPSCl composite after the 4 V charge show little evidence of the $FePO_4$ (FP) phase (**Figure S8a**) while the LZC composite shows signs of the expected FP phases formed (**Figure S8c**). Undetectability of the FP phase supports the low-capacity utilization percentage of 65.4% with LPSCl. It should be noted that a percentage of this capacity is attributed to SSE oxidation and not necessarily de-lithiation of the cathode. Detectability of the FP phase within the bulk cathode composite reinforces the capacity utilization percentage of 83.7% with LZC. In addition, Raman spectra also reinforce these findings where peaks attributed to FP vibrational modes are present for the LZC case at 189 cm^{-1}, 305 cm^{-1}, and 335 cm^{-1} (**Figure S8d**), as assigned in prior work.[51] Bulk properties of the LPSCl cathode composite in the charged state reveal that electrolyte oxidation inhibits lithium transport during de-lithiation. LFP particle volume change of ~6.0%[52] and the poor densification of LPSCl can cause additional void formation leading to reduced interfacial contact. Any intimate interface further degrades when interfacial oxidation products like sulfur and phosphorus sulfides are generated as confirmed by XPS.

After oxidation products were confirmed and identified, electrochemical impedance spectroscopy (EIS) was conducted to quantify the impedance growth within the cathode composite during cycling. With the LFP/LPSCl composite, EIS was conducted after the first and third cycle where the capacity appears to have stabilized, and the data were fitted using the following equivalent circuit shown in **Figure 5a**. The high-frequency region can be assigned to the bulk SSE resistance. The intermediate frequency range is attributed to the cathode electrolyte interface (CEI) and the low-frequency region is assigned to the charge transfer (CT) resistance.[50,51] Fitting results shown in **Figure 5b**, show resistance contributions where after the first cycle, 96 Ω is assigned to the CEI growth and 505 Ω is assigned to CT. After the third cycle, we observe a large growth in both CEI and CT, confirming that with subsequent cycling, LPSCl oxidation products and poor interfacial contact caused by a porous composite lead to large impedance growth even just after the third cycle. This supports the electrochemical performance results, where for the third cycle, a low discharge capacity of 27 mAh g^{-1} is obtained (**Figure 3a**).

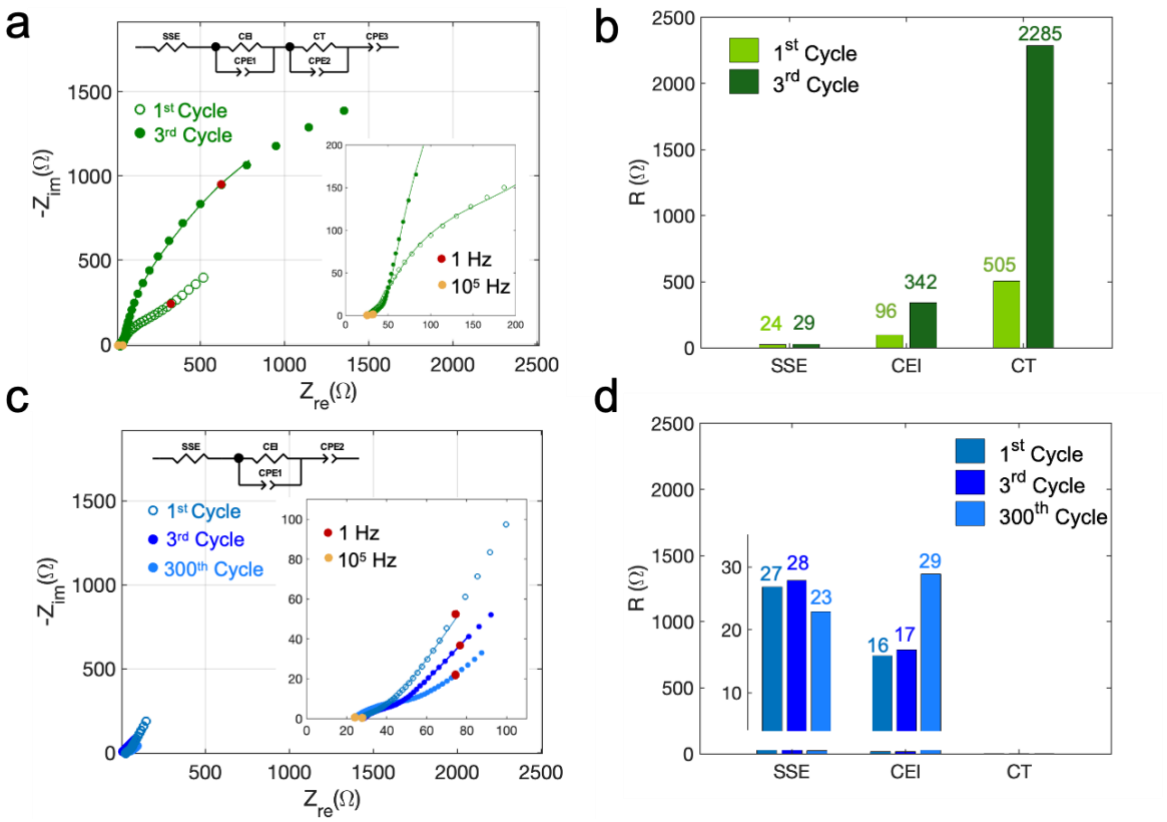

Figure 5. Nyquist plots and equivalent circuit fitting results from electrochemical impedance spectroscopy measurements for a-b) LPSCl and c-d) LZC.

With the LFP/LZC cathode, EIS was conducted after the 1st, 3rd, and 300th cycle, showing that impedance growth after extended cycling grows marginally. EIS results were fitted to the following circuit shown in **Figure 5c**, where the high-frequency range is attributed to the bulk SSE resistance and intermediate frequency region is assigned to the CEI. We do observe that the bulk SSE resistance is higher for the LZC composite than the LPSCl, since LPSCl exhibits higher ionic conductivity. Fitting results shown in **Figure 5d** show that after the first cycle, CEI resistance is 16 Ω with marginal growth after 300 cycles to 29 Ω. Even after 300 cycles, the CEI resistance of the LFP/LZC composite is less than LFP/LPSCl even after the first cycle. The complete EIS fitting results for both composites are shown in **Table S1**. Quantifying the

impedance of the cathode composites after cycling confirm the hypothesis that for the LPSCl case, oxidation products are generated after the first charge. These oxidation products inhibit lithium-ion transport leading to large impedance growth, attributed to CEI growth during subsequent cycling. Due to the high oxidative stability of LZC and good interfacial contact, impedance growth with extended cycling is negligible, leading to an improved electrochemical performance at high rates.

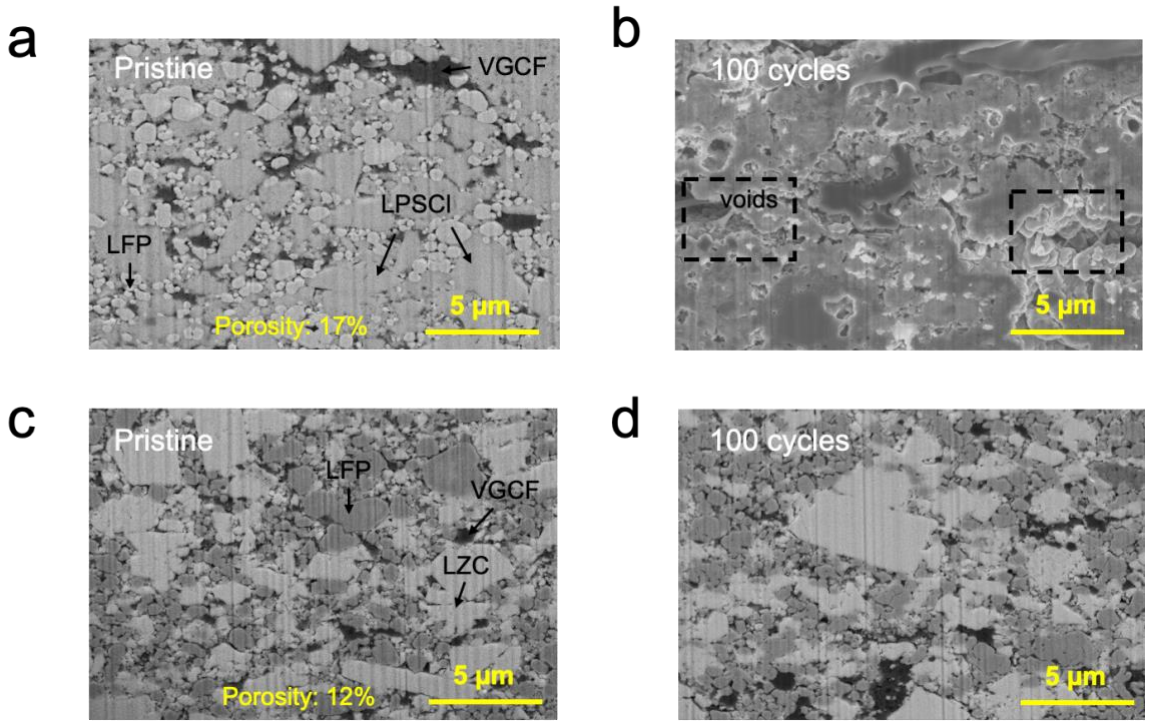

Figure 6. FIB-SEM cross sections of pristine and cycled LFP/SSE composites with a), b) LPSCl and c), d) LZC electrolytes at the discharged state.

To analyze interfacial degradation and morphology, FIB cross-sections were obtained of the post-cycled LFP/SSE cathode composites as shown in **Figure 6**. Compared to the pristine LFP/LPSCl composite (**Figure 6a**), its cycled counterpart (**Figure 6b**) displays clear evidence of voids and poor interfacial contact likely attributed to the formation of interfacial decomposition

products, LFP volume change, and the poor densification of LPSCl. Since the solid-state system is physically constrained, expansion and contraction of the cathode particles cause internal stresses on the solid electrolyte. If the solid electrolyte exhibits reduced deformability, like LPSCl compared to LZC, as shown in **Figure 2**, intimate contact will degrade with consecutive cycling. These results help explain the large impedance growth and electrochemical performance with LPSCl. However, with the LFP/LZC composite, morphology and interfacial contact are well preserved after 100 cycles (**Figure 6c and 6d**), and even after the charged state (**Figure S9**) where no clear changes are observed. Preservation of the LFP/LZC interface assists in elucidating the improved electrochemical performance and marginal impedance growth with cycling.

In this work, sulfide and chloride solid electrolytes were investigated to elucidate the critical interfacial challenges of nanoscale carbon-coated LFP in ASSBs. With the sulfide-based LPSCl, poor oxidative stability and incompatibility with high surface area carbon-coated LFP caused excessive electrolyte oxidation forming elemental sulfur and phosphorus sulfides which inhibited lithium transport and led to large impedance growth during cycling. This resulted in poor electrochemical performance and shed light on why numerous prior works on solid-state LFP chemistries required the use of polymers or liquid additives. In contrast, with the chloride-based LZC, high oxidative stability and mechanical deformability facilitated a stable and passivating interface and good interfacial contact, resulting in marginal impedance growth with subsequent cycling. The stable interface between LFP and LZC enabled extended cycling performance of 1000 cycles (80% retention) at 1C without requiring elevated temperature conditions. These results showcase the importance of interfacial cathode composite design for

high-performance ASSBs, and highlight the need to consider the cathode's morphological, surface as well as electrochemical properties in future SSE selection methodology.

ASSOCIATED CONTENT

Supporting Information.

Experimental methods, Reitveld refinements, ionic and electronic conductivities of LPSCl and LZC, Nyquist plots, image processing of densified pellets from FIB-SEM, experimental data of cathodes and cathode composites including XRD, Raman, FIB-SEM, additional electrochemical data, Nyquist plots, and corresponding fitting results.

Corresponding Author

Ying Shirley Meng – Department of NanoEngineering, University of California San Diego, La Jolla, CA, 92093, United States, and Pritzker School of Molecular Engineering, The University of Chicago, Chicago, IL, 60637, United States

Email: shirleymeng@uchicago.edu

Darren H.S. Tan - Department of NanoEngineering, University of California San Diego, La Jolla, CA, 92093, United States

Email: dht020@eng.ucsd.edu

Authors

Ashley Cronk – Materials Science and Engineering Program, University of California San Diego, La Jolla, CA, 92093, United States

Yu-Ting Chen – Materials Science and Engineering Program, University of California San Diego, La Jolla, CA, 92093, United States

Grayson Deysher – Materials Science and Engineering Program, University of California San Diego, La Jolla, CA, 92093, United States

So-Yeon Ham – Materials Science and Engineering Program, University of California San Diego, La Jolla, CA, 92093, United States

Hedi Yang – Department of NanoEngineering, University of California San Diego, La Jolla, CA, 92093, United States

Phillip Ridley – Department of NanoEngineering, University of California San Diego, La Jolla, CA, 92093, United States

Baharak Sayahpour – Materials Science and Engineering Program, University of California San Diego, La Jolla, CA, 92093, United States

Long Hoang Bao Nguyen – Department of NanoEngineering, University of California San Diego, La Jolla, CA, 92093, United States

Jin An Sam Oh – Department of NanoEngineering, University of California San Diego, La Jolla, CA, 92093, United States

Jihyun Jang – Department of NanoEngineering, University of California San Diego, La Jolla, CA, 92093, United States

Darren H. S. Tan – Department of NanoEngineering, University of California San Diego, La Jolla, CA, 92093, United States

Notes

The authors declare the following financial interests/personal relationships which may be considered as potential competing interests: Ying Shirley Meng reports financial support was provided by LG Energy Solution.

ACKNOWLEDGMENT

A.C. acknowledges the National Science Foundation for having supported her Ph.D. research through the NSF Graduate Research Fellowship Program. This work was funded by the LG Energy Solution through the Frontier Research Laboratory (FRL) Program. The authors acknowledge the support of UNIGRID Battery, a UCSD spin-out company for fruitful discussions. The authors would also like to acknowledge the UCSD Crystallography Facility. This work was performed in part at the San Diego Nanotechnology Infrastructure (SDNI) of UCSD, a member of the National Nanotechnology Coordinated Infrastructure, which is supported by the National Science Foundation (Grant ECCS-1542148), along with the use of facilities and instrumentation supported by NSF through the UC San Diego Materials Research Science and Engineering Center (UCSD MRSEC), grant #DMR-201192. The authors acknowledge the use of facilities and instrumentation at the UC Irvine Materials Research Institute (IMRI), which is supported in part by the National Science Foundation through the UC Irvine Materials Research Science and Engineering Center (DMR-2011967), Specifically, the XPS work was performed using instrumentation funded in part by the National Science Foundation Major Research Instrumentation Program under grant No. CHE-1338173.

REFERENCES

1) Zubi, G.; Dufo-López, R.; Carvalho, M.; Pasaoglu, G. The lithium-ion battery: State of the art and future perspectives. *Renewable and Sustainable Energy Reviews.* **2018***,* vol. 89 292–308, DOI: 10.1016/j.rser.2018.03.002

2) Stampatori, D.; Raimondi, P. -P.; Noussan, M. Li-ion batteries: A review of a key technology for transport decarbonization. *Energies (Basel).* **2020***,* 13 (10) 2638, DOI: 10.3390/ en13102638

3) Olivetti, E.-A.; Ceder, G.; Gaustad, G.-G.; Fu, X. Lithium-Ion Battery Supply Chain Considerations: Analysis of Potential Bottlenecks in Critical Metals. *Joule.* **2017***,* vol. 1 229–243, DOI: 10.1016/j.joule.2017.08.019

4) Halm, I. Surging commodity prices could impact the growth of the EV sector. *Mining Technology,* **2022***. https://www.mining-technology.com/analysis/commodity-prices-ev-sector-growth/*

5) Murdock, B.-E.; Toghill, K. E.; Tapia-Ruiz, N. A Perspective on the Sustainability of Cathode Materials used in Lithium-Ion Batteries. *Advanced Energy Materials.* **2021***,* 11, DOI: 10.1002/aenm.202102028

6) Padhi, A.-K.; Nanjundaswamy, K.-S.; Goodenough, J.-B. Phospho-olivines as Positive-Electrode Materials for Rechargeable Lithium Batteries. *J. Electrochem. Soc.* **1997***,* vol. 144, 1188-1194

7) Coppola, G.; Baker R.-D. Tesla Shifting to Cheaper Battery Chemistry Tried in China. *Bloomberg US Edition.* **2021**.

8) Kolodny, L. Rivian will follow Tesla and change the type of battery cells it uses in standard packs. *CNBC.* **2022**.

9) BloombergNEF. Lithium-Ion Batteries: 2021 State of the Industry Analysis, Long-Term Energy Storage Outlook, Long-Term Electric Vehicle Outlook and 2020 Lithium-Ion Battery Price Survey. **2021**. *https://about.newenergyfinance.com/electric-vehicle-outlook/*

10) BloombergNEF. Lithium-Ion Batteries: 2022 Electric Vehicle Outlook. **2022**.

11) Hu, J.; Huang, W.; Yang, L.; Pan, F. Structure and performance of the $LiFePO_4$ cathode material: From the bulk to the surface. *Nanoscale.* **2020***,* vol. 12, 15036–15044, DOI: 10.1039/d0nr03776a

12) Hess, M.; Sasaki, T.; Villevieille, C.; Novák, P. Combined operando X-ray diffraction-electrochemical impedance spectroscopy detecting solid solution reactions of $LiFePO_4$ in batteries. *Nat Commun.* **2015***,* 6, 8169, DOI: 10.1038/ncomms9169

13) Feng, X.; Ouyang, M.*;* Liu, X.; Lu, L.; Xia, Y.; He, X. Thermal runaway mechanism of lithium-ion battery for electric vehicles: A review. *Energy Storage Materials.* **2018***,* 10, 246–267 DOI: 10.1016/j.ensm.2017.05.013

14) Oh, D.-Y.*;* Nam, Y.-J.; Park, K.-H.; Jung, S.-H.; Cho, S.-J.; Kim, Y.-K.; Lee, Y.-G.; Lee, S.-Y.; Jung, Y.-S. Excellent Compatibility of Solvate Ionic Liquids with Sulfide Solid Electrolytes: Toward Favorable Ionic Contacts in Bulk-Type All-Solid-State Lithium-Ion Batteries. *Adv Energy Mater.* **2015***,* 5, 1500865, DOI: 10.1002/aenm.201500865

15) Yan, X.; Li, Z.; Wen, Z.; Han, W. $Li/Li_7La_3Zr_2O_{12}/LiFePO_4$ all-solid-state battery with ultrathin nanoscale solid electrolyte. *Journal of Physical Chemistry C.* **2017***,* 121, 1431–1435.

16) Wang, Z.; Tan, R.; Wang, H.; Yang, L.; Hu, J.; Chen, H.; Pan, F. A Metal–Organic-Framework-Based Electrolyte with Nanowetted Interfaces for High-Energy-Density Solid-State Lithium Battery. *Advanced Materials.* **2018***,* 30.

17) Ma, C.; Dai, K.; Hou, H.; Ji, K.; Chen, L.; Ivey, D.; Wei, W. High Ion-Conducting Solid-State Composite Electrolytes with Carbon Quantum Dot Nanofillers. *Advanced Science.* **2018***,* 5, 1700996.

18) Zeng, H.; Ji, X.; Tsai, F.; Zhang, Q.; Jiang, T.; Li, R.; Shi, H.; Luan, S.; Shi, D. Enhanced cycling performance for all-solid-state lithium-ion battery with $LiFePO_4$ composite cathode encapsulated by poly (ethylene glycol) (PEG) based polymer electrolyte. *Solid State Ionics.* **2018***,* 320, 92–99.

19) Xu, H.; Chien, P.; Shi, J.; Li, Y.; Wu, N.; Liu, Y.; Hu, Y.; Goodenough, J. High-performance all-solid-state batteries enabled by salt bonding to perovskite in poly(ethylene oxide). *Proc Natl Acad Sci U S A.* **2019***,* 116, 18815–18821.

20) Wang, S.; Li, S.; Wei, B.; Lu, X. Interfacial Engineering at Cathode/LATP Interface for High-Performance Solid-State Batteries. *J Electrochem Soc.* **2020***,* 167, 100528.

21) Yang, C.; Wu, Q.*;* Xie, W.; Zhang, X.; Brozena A.; Zheng, J.; Garaga, M.; Ko, B.; Mao, Y.; He, S.; Gao, Y.; Wang, P.; Tyagi, M.; Jiao, F.; Briber, R.; Albertus, P.; Wang, C.; Greenbaum, S.; Hu, Y.; Isogai, A.; Winter, M.; Xu, K.; Qi, Y.; Hu, L. Copper-coordinated cellulose ion conductors for solid-state batteries. *Nature.* **2021***,* 598, 590–596.

22) Zagórski, J.; Silván, B.; Saurel, D.; Aguesse, F.; Llordés, A. Importance of Composite Electrolyte Processing to Improve the Kinetics and Energy Density of Li Metal Solid-State Batteries. *ACS Appl Energy Mater.* **2020***,* 3, 8344–8355.

23) Erabhoina, H.; Thelakkat, M. Tuning of composition and morphology of $LiFePO_4$ cathode for applications in all solid-state lithium metal batteries. *Sci Rep.* **2020**. 12, 1.

24) Li, J.; Qi, J.; Jin, F.; Zhang, L.; Tang, L.; Huang, R.; Xu, J.; Chen, H.; Liu, M.; Qiu, Y.; Cooper, A.; Shen, Y.; Chen, L. Room temperature all-solid-state lithium batteries

based on a soluble organic cage ionic conductor. *Nat Commun.* **2022.** 13 (1), DOI: 10.1038/41467-022-29743-1

25) Chen, H.; Yu, L.; Cao, X.; Yang, Q.; Liu, Y.; Wei, Y.; Zeng, J.; Zhong, L.; Qiu, Y. The multicomponent synergistic effect of a hierarchical $Li_{0.485}La_{0.505}TiO_3$ solid-state electrolyte for dendrite-free lithium-metal batteries. *Nanoscale.* **2022,** 14, 7766–7777.

26) Rosenbach, D.; Krimalowski, A.; Erabhoina, H.; Thelakkat, M. Solid polymer electrolytes from polyesters with diester sidechains for lithium metal batteries. *J Mater Chem A Mater.* **2022**, DOI:10.1039/d2ta00800a.

27) Tatsumisago, M.; Nagao, M.; Hayashi, A. Recent development of sulfide solid electrolytes and interfacial modification for all-solid-state rechargeable lithium batteries. *Journal of Asian Ceramic Societies.* **2013***,*1 17–25, DOI: 10.1016/j.jascer.2013.03.005

28) Bai, X.; Duan, Y.; Zhuang, W.; Yang, R.; Wang, J. Research progress in Li-argyrodite-based solid-state electrolytes. *Journal of Materials Chemistry A.* **2020***,* 8, 25663–25686 DOI: 10.1039/d0ta08472g

29) Chen, Y.-T.; Marple, M.; Tan, D.; Ham, S.; Sayahpour, B.; Li, W.; Yang, H.; Lee, J.; Hah, H.; Wu, E.; Doux, J.; Jang, J.; Ridley, P.; Cronk, A.; Deysher, G.; Chen, Z.; Meng, Y. Investigating dry room compatibility of sulfide solid-state electrolytes for scalable manufacturing. *J Mater Chem A Mater.* **2022***,* 10, 7155–7164

30) Byeon, Y.-W.; Kim, H. Review on Interface and Interphase Issues in Sulfide Solid-State Electrolytes for All-Solid-State Li-Metal Batteries. *Electrochem.* **2021***,* 2, 452–471.

31) Wu, E.-A.; Jo, C.; Tan, D.-H.-S.; Zhang, M.; Doux, J.; Chen, Y.; Deysher, G.; Meng, Y.-S. A Facile, Dry-Processed Lithium Borate-Based Cathode Coating for Improved All-Solid-State Battery Performance. *J Electrochem Soc.* 2020. **167**, 130516.

32) Kitsche, D.; Tang, Y.; Ma, Y.; Goonetilleke, D.; Sann, J.; Walther, F.; Bianchini, M.; Janek, J.; Brezesinski. High Performance All-Solid-State Batteries with a Ni-Rich NCM Cathode Coated by Atomic Layer Deposition and Lithium Thiophosphate Solid Electrolyte. *ACS Appl Energy Mater.* **2021**, 4, 7338–7345.

33) Culver, S. P.; Koerver, R.; Zeier, W.-G.; Janek, J. On the Functionality of Coatings for Cathode Active Materials in Thiophosphate-Based All-Solid-State Batteries. *Advanced Energy Materials.* **2019,** 9. DOI:10.1002/aenm.201900626.

34) Kwak, H.-W.; Park, Y.-J. Cathode coating using $LiInO_2$-LiI composite for stable sulfide-based all-solid-state batteries. *Sci Rep.* **2019***,* 9, 8099, DOI: 10.1038/s41598-019-44629-x

35) Tan, D.-H.-S.; Banerjee, A.; Chen, Z; Meng, Y.-S. From nanoscale interface characterization to sustainable energy storage using all-solid-state batteries. *Nat Nanotechnol.* **2020.** 15, 170–180.

36) Li, X. *et al.* Progress and perspectives on halide lithium conductors for all-solid-state lithium batteries. *Energy and Environmental Science.* **2020**, 13, 1429–1461, DOI:1039/c9ee03828k

37) Kato, A.;Yamamoto, M.; Sakuda, A.; Hayashi, A.; Tatsumisago, M. Mechanical Properties of Li_2S-P_2S_5 Glasses with Lithium Halides and Application in All-Solid-State Batteries. *ACS Appl Energy Mater.* **2018***,* 1, 1002–1007.

38) Asano, T.; Sakai, A.; Ouchi, S.; Sakaida, M.; Miyazaki, A.; Hasegawa, S. Solid Halide Electrolytes with High Lithium-Ion Conductivity for Application in 4 V Class Bulk-Type All-Solid-State Batteries. *Advanced Materials.* **2018***,* 30, 1803075.

39) Li, X.; Liang, J.; Luo, J.; Norouzi Banis, M.; Wang, C.; Li, W.; Deng, S.; Yu, C.; Zhao, F.; Hu, Y.; Sham, T.; Zhang, L.; Zhao, S.; Lu, S.; Huang, H.; Li, R.; Adair, K.; Sun, X. Air-stable Li_3InCl_6 electrolyte with high voltage compatibility for all-solid-state batteries. *Energy Environ Sci.* **2019***,* 12, 2665–2671.

40) Kwak, H.; Han, D.; Lyoo, J.; Park, J.; Jung, S.; Han, Y.; Kwon, G.; Kim, H.; Hong, S.; Nam, K.; Jung, Y.-S. New Cost-Effective Halide Solid Electrolytes for All-Solid-State Batteries: Mechanochemically Prepared Fe^{3+}-Substituted Li2ZrCl6. *Adv Energy Mater.* **2021***,* 11, 2003190.

41) Kim, S.-Y.; Kaup, K.; Park, K.-H.; Assoud, A.; Zhou, L.; Liu, J.; Wu, X.; Nazar, L.-F. Lithium Ytterbium-Based Halide Solid Electrolytes for High Voltage All-Solid-State Batteries. *ACS Mater Lett.* **2021***,* 3, 930–938.

42) Park, K.-H.; Kavish, K.; Assoud, A.; Zhang, Q.; Wu, X.; Nazar, L.-F. High-Voltage Superionic Halide Solid Electrolytes for All-Solid-State Li-Ion Batteries. *ACS Energy Lett.* **2020***,* 533–539, DOI:10.1021/acsenergylett.9b02599.

43) Cao, D.; Zhang, Y.; Nolan, A.; Sun, X.; Liu, C.; Sheng, J.; Mo, Y.; Wang, Y.; Zhu, H. Stable Thiophosphate-Based All-Solid-State Lithium Batteries through Conformally Interfacial Nanocoating. *Nano Lett.* **2020***,* 20, 1483–1490.

44) Banerjee, A.; Wang, X.; Fang, C.; Wu, E.-A.; Meng, Y.-S. Interfaces and Interphases in All-Solid-State Batteries with Inorganic Solid Electrolytes. *Chemical Reviews.* **2020***,* 120, 6878–6933, DOI:10.1021/acs.chemrev.0c00101

45) Doux, J.-M., Yang, Y.; Tan, D.-H.-S.; Nguyen, H.; Wu, E.-A.; Wang, X.; Banerjee, A.; Meng, Y.-S. Pressure effects on sulfide electrolytes for all solid-state batteries. *J Mater Chem A Mater*. **2020**. 8, 5049–5055.

46) Zhang, W.; Leichtweiß, T.; Culver, S.-P.; Koerver, R.; Das, D.; Weber, D.-A.; Zeier, W.-G.; Janek, J. The Detrimental Effects of Carbon Additives in $Li_{10}GeP_2S_{12}$-Based Solid-State Batteries. *ACS Appl Mater Interfaces.* **2017***,* 9, 35888–35896

47) Auvergniot, J.; Cassel, A.; Ledeuil, J.; Viallet, V.; Seznec, V.; Dedryvere, R. Interface Stability of Argyrodite Li_6PS_5Cl toward $LiCoO_2$, $LiNi_{1/3}Co_{1/3}Mn_{1/3}O_2$, and $LiMn_2O_4$ in Bulk All-Solid-State Batteries. *Chemistry of Materials.* **2017***,* 29, 3883–3890

48) Wu, J.; Krishna, G.; Dathar, P.; Sun, C.; Theivanayagam, M.-G.; Applestone, D.; Dylla, A.-G.; Manthiram, A.; Henkelman, G.; Goodenough, J.-B.; Stevenson, K. In situ Raman spectroscopy of $LiFePO_4$: Size and morphology dependence during charge and self-discharge. *Nanotechnology.* **2013***,* 24, 42.

49) Okubo, M.; Asakura, D.; Mizuno, Y.; Kim, J.; Mizokawa, T.; Kudo, T.; Honma, I. Switching redox-active sites by valence tautomerism in prussian blue analogues $A_xMn_y[Fe(CN)_6]\cdot$ n H_2O (A: K, Rb): Robust frameworks for reversible Li storage. *Journal of Physical Chemistry Letters.* **2010***,* 1, 2063–2071.

50) Mei, B.-A.; Munteshari, O.;Lau, J.; Dunn, B.; Pilon, L. Physical Interpretations of Nyquist Plots for EDLC Electrodes and Devices. *Journal of Physical Chemistry C.* **2018***,* 122, 194–206.

51) Asano, T.; Yubuchi, S.; Sakuda, A.; Hayashi, A.; Tatsumisago, M. Electronic and Ionic Conductivities of $LiNi_{1/3}Mn_{1/3}Co_{1/3}O_2$ -Li_3PS_4 Positive Composite Electrodes for All-Solid-State Lithium Batteries. *J Electrochem Soc.* **2017***,* 164, A3960–A3963.